

# X-ray nano-imaging of defects in thin film catalysts via cluster analysis

Cite as: Appl. Phys. Lett. **121**, 153904 (2022); <https://doi.org/10.1063/5.0125268>

Submitted: 10 September 2022 • Accepted: 11 September 2022 • Published Online: 11 October 2022

 Aileen Luo,  Oleg Yu. Gorobtsov,  Jocienne N. Nelson, et al.



View Online



Export Citation



CrossMark

## ARTICLES YOU MAY BE INTERESTED IN

[Measurements of thermoelectric figure of merit based on multi-harmonic thermal analysis of thermographic images](#)

Applied Physics Letters **121**, 154104 (2022); <https://doi.org/10.1063/5.0105282>

[Characterization of hole traps in reverse-biased Schottky-type p-GaN gate HEMTs by current-transient method](#)

Applied Physics Letters **121**, 153501 (2022); <https://doi.org/10.1063/5.0107459>

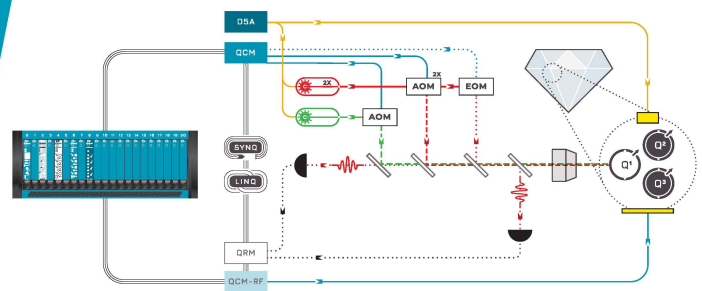
[Mechanically tunable elastic modulus of freestanding  \$\text{Ba}\_{1-x}\text{Sr}\_x\text{TiO}\_3\$  membranes via phase-field simulation](#)

Applied Physics Letters **121**, 152902 (2022); <https://doi.org/10.1063/5.0099772>

 QBLOX

Integrates all  
Instrumentation + Software  
for Control and Readout of  
**NV-Centers**

[visit our website >](#)



# X-ray nano-imaging of defects in thin film catalysts via cluster analysis

Cite as: Appl. Phys. Lett. **121**, 153904 (2022); doi: [10.1063/5.0125268](https://doi.org/10.1063/5.0125268)

Submitted: 10 September 2022 · Accepted: 11 September 2022 ·

Published Online: 11 October 2022



View Online



Export Citation



CrossMark

Aileen Luo,<sup>1,a)</sup>  Oleg Yu. Gorobtsov,<sup>1</sup> Jocienne N. Nelson,<sup>2,b)</sup>  Ding-Yuan Kuo,<sup>1</sup> Tao Zhou,<sup>4</sup> Ziming Shao,<sup>1</sup> Ryan Bouck,<sup>1</sup> Mathew J. Cherukara,<sup>4,c)</sup>  Martin V. Holt,<sup>4</sup> Kyle M. Shen,<sup>5,6</sup>  Darrell C. Schlom,<sup>1,6,7</sup>  Jin Suntivich,<sup>1</sup>  and Andrej Singer<sup>1</sup> 

## AFFILIATIONS

<sup>1</sup>Department of Materials Science and Engineering, Cornell University, Ithaca, New York 14853, USA

<sup>2</sup>Laboratory of Atomic and Solid State Physics, Department of Physics, Cornell University, Ithaca, New York 14853, USA

<sup>3</sup>Advanced Photon Source, Argonne National Laboratory, Lemont, Illinois 60439, USA

<sup>4</sup>Center for Nanoscale Materials, Argonne National Laboratory, Lemont, Illinois 60439, USA

<sup>5</sup>Department of Applied and Engineering Physics, Cornell University, Ithaca, New York 14853, USA

<sup>6</sup>Kavli Institute at Cornell for Nanoscale Science, Ithaca, New York 14853, USA

<sup>7</sup>Leibniz-Institut für Kristallzüchtung, Max-Born-Str. 2, 12489 Berlin, Germany

<sup>a)</sup> Author to whom correspondence should be addressed: [al2493@cornell.edu](mailto:al2493@cornell.edu)

<sup>b)</sup> Present address: National Renewable Energy Laboratory, Golden, Colorado 80401, USA.

<sup>c)</sup> Present address: Advanced Photon Source, Argonne National Laboratory, Lemont, Illinois 60439, USA.

## ABSTRACT

Functional properties of transition-metal oxides strongly depend on crystallographic defects; crystallographic lattice deviations can affect ionic diffusion and adsorbate binding energies. Scanning x-ray nanodiffraction enables imaging of local structural distortions across an extended spatial region of thin samples. Yet, localized lattice distortions remain challenging to detect and localize using nanodiffraction, due to their weak diffuse scattering. Here, we apply an unsupervised machine learning clustering algorithm to isolate the low-intensity diffuse scattering in as-grown and alkaline-treated thin epitaxially strained SrIrO<sub>3</sub> films. We pinpoint the defect locations, find additional strain variation in the morphology of electrochemically cycled SrIrO<sub>3</sub>, and interpret the defect type by analyzing the diffraction profile through clustering. Our findings demonstrate the use of a machine learning clustering algorithm for identifying and characterizing hard-to-find crystallographic defects in thin films of electrocatalysts and highlight the potential to study electrochemical reactions at defect sites in operando experiments.

Published under an exclusive license by AIP Publishing. <https://doi.org/10.1063/5.0125268>

Limited natural resources and increasing demand for sustainable energy create a need for efficient electrochemical energy conversion and storage devices, such as batteries, fuel cells, and electrolyzers. Crystallographic defects are critical for a broad range of material functionalities,<sup>1</sup> and the role of defects in electrochemical systems has attracted considerable attention. For example, the crystallographic orientation of electrocatalysts significantly impacts catalytic activity due to the differences in electronic structures associated with surface termination facets.<sup>2–4</sup> Additionally, a manipulation of the surface concentration of the A-site cation in ABO<sub>3</sub> perovskites during synthesis mitigates activity inhibition due to point defects in the form of surface cation segregation.<sup>5</sup>

Unlike facets and homogeneously distributed vacancies, the effect of crystalline line defects (dislocations), partial amorphization,

non-uniform film thickness, or point defect clusters on catalytic activity is poorly understood. In non-oxide materials, the strain gradients around dislocations were discussed early on;<sup>6</sup> however, the lack of operando access to structural information has prevented further forays in this direction, partly due to challenges in developing an operando imaging method with a resolution of tens of nanometers to probe the distortions produced by dislocations.<sup>7</sup> While environmental and operando transmission electron microscopy (TEM) provide atomic resolution information on various catalytic materials,<sup>8–10</sup> side reactions with the electron beam in liquid cells may affect the systems' dynamics, and typically, only small specimens can be investigated. Surface-sensitive operando atomic force microscopy (AFM) measures changes in surface topography and electrochemical potentials during energy conversion processes such as the oxygen evolution reaction (OER).<sup>11,12</sup>

Nonetheless, AFM and optical methods using super-resolution<sup>13</sup> lack direct information about lattice distortions.

Identifying localized structural distortions with x-ray diffraction coupled with x-ray fluorescence spectroscopy is a potential way to directly investigate the catalytic activity in proximity to defects. By combining the analysis with the sophisticated atomic deposition technology of thin films, the impact of inhomogeneities at the hundreds of nanometers length scale can be distinguished from defects such as grain boundaries (often absent in epitaxial films) and vacancy orderings (likely too small to be probed with x rays). X-ray nanodiffraction enables the study of large distortions in epitaxial thin films, such as phase distribution in materials with a metal–insulator transition.<sup>14</sup> Yet, imaging more subtle localized lattice distortions remains challenging because the signal associated with minute distortions is difficult to isolate and interpret. Here, we combined synchrotron-based x-ray diffraction nanoimaging with machine learning and simulations to categorize heterogeneities in compressively strained SrIrO<sub>3</sub> epitaxial thin films, a promising catalyst material for electrochemical conversion in acidic and alkaline solutions.<sup>15,16</sup> We collected 4D scanning data and used k-means clustering to localize regions with lattice imperfections (to 50 nm precision, see Methods in the [supplementary material](#)), which we attribute to strain fields around dislocation half-loops. Furthermore, we find that the strain gradient morphology in a film electrochemically treated under alkaline conditions differs from the morphology in the pristine film. This suggests that electrochemical treatment modifies strain morphology, emphasizing the need for future operando measurements.

**Figure 1(a)** shows a schematic of the experimental geometry. The in-plane lattice parameters of the epitaxially grown 12 nm thin SrIrO<sub>3</sub> films used in this study are coherently strained to those of the (LaAlO<sub>3</sub>)<sub>0.3</sub>(SrAl<sub>0.5</sub>Ta<sub>0.5</sub>O<sub>3</sub>)<sub>0.7</sub> (LSAT) substrate crystal [see diffraction of 103<sub>pc</sub> peak in Fig. S1(D) of the [supplementary material](#)]. Because of the lattice mismatch, the out-of-plane lattice parameter of the film differs from that of the substrate, allowing us to isolate the specular 002<sub>pc</sub> Bragg reflection (pc: pseudocubic) of the film from the much stronger substrate reflection. **Figure 1(b)** shows the reciprocal space around the 002<sub>pc</sub> Bragg peak taken with a 0.5 × 0.5 mm<sup>2</sup> unfocused x-ray beam in the pristine (as-grown) SrIrO<sub>3</sub> film. The well-defined, uniform thickness of the film introduces thickness fringes around the Bragg peak perpendicular to the film surface, and crystal defects—deviations from a periodic crystal—result in diffuse scattering around the peak.

To capture the spatial distribution of the defects, we raster-scanned a focused 30 nm diameter x-ray beam over an area of the SrIrO<sub>3</sub> thin film and recorded 2D diffraction images at each point in the 2D plane of the scan, collectively forming a 4D dataset [**Fig. 1(a)**]. The scattering geometry used here increases the horizontal footprint of the beam by a factor of 1/sin( $\theta$ ), where  $\theta = 15.87^\circ$  is the incident angle. We collected scans at three different  $\theta$ -2 $\theta$  values to record the diffuse scattering profile in the reciprocal space: at the Bragg condition and incident angles offset by  $\Delta\theta = \pm 0.2^\circ$  (rocking width  $\sim 0.4^\circ$ ). Through varying the incident angle, a portion of broad diffuse scattering is measurable at the same scattering angle 2 $\theta$ , while the position of the sharp Bragg peak changes [**Fig. 1(c)**] because the Ewald sphere intercepts the sharp Bragg truncation rod at a different scattering vector  $Q$  [**Fig. 1(b)**]. The highest intensity measured displays a “donut-shaped” ring: a real image of the Fresnel zone plate focusing the x-ray

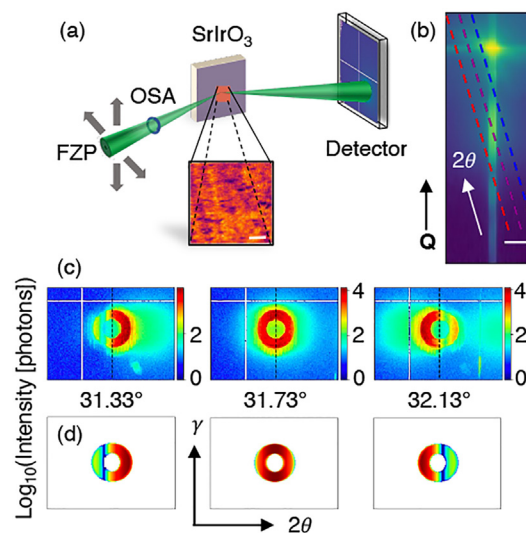


**FIG. 1.** (a) Schematic illustration of the focused nano-probe diffraction geometry (scale bar: 1  $\mu\text{m}$ ). (b) SrIrO<sub>3</sub> 002<sub>pc</sub> Bragg peak with lines indicating the different cuts of the Ewald sphere as measured at incident angles of 15.67° (red), 15.87° (purple), and 16.07° (blue). Scale bar: 0.11 nm<sup>-1</sup>. (c) Total diffraction intensity integrated over a raster scan across a region of the sample at incident angles of  $\theta = 15.67^\circ$  (left),  $\theta = 15.87^\circ$  (middle), and  $\theta = 16.07^\circ$  (right). Each diffraction image spans 1.32° in 2 $\theta$ . (d) Simulated total diffraction intensity from a perfect film normalized to the experimental data, where the vertical drop in intensity (left, right, visible as a blue stripe in the false color images) shows the first minimum in the Laue oscillations originating from film thickness. The diffuse scattering visible in the experimental data is missing in the simulation.

beam (a beamstop blocks the central intensities, the focusing generates a divergent x-ray beam at the sample,<sup>17</sup> and the high quality thin film acts as a mirror in Bragg reflection). At the exact Bragg condition, a complete ring is visible due to the small thickness of the film, resulting in diffraction within a range of incident angles [**Fig. 1(c)**, middle]. Thus, the intensity contained within the ring primarily comes from the Bragg diffraction condition. In the off-Bragg data, the donut shape exhibits a wide vertical shadow at lower and higher 2 $\theta$  [**Figs. 1(c)** and **1(d)**, left and right, respectively] due to the minimum between the Laue oscillations present in diffraction from a high-quality thin film [**Fig. 1(b)**]. The diffuse scattering is more discernable in the off-Bragg measurements as a broad background outside the ring, with total intensity two orders of magnitude lower than the donut-shaped peak.

One of the primary benefits of the increased brilliance of synchrotron light sources and upgraded photon detectors is the high speed at which data are collected. The massive amounts of data present a challenge in x-ray science: efficient and effective data processing. **Figure 1(a)** shows the map of the total intensity from the pristine SrIrO<sub>3</sub> thin film obtained by summing the total intensity from the 2D diffraction pattern collected at each spatial position, thereby creating a four-dimensional (4D) dataset (2D detector image at every step of a 2D raster scan) from single angle diffraction. While the integrated intensity displays some features in the film, it lacks the signatures of the features in the reciprocal space. This method of condensing 4D data into 2D loses the nuance of the full diffraction patterns. The scattering signal is inhomogeneously distributed across the measured slice of the Ewald

sphere within one diffraction pattern, let alone across the extended spatial region of the sample. Often, nanodiffraction data analysis resembles dark-field imaging with manual identifying regions in the reciprocal space corresponding to different local structures.<sup>14</sup> Yet, the method is inapplicable to the low-signal diffuse scattering.

Here, we used k-means clustering—an unsupervised machine learning algorithm—to categorize the data by the intensity at each pixel position on the detector. K-means clustering is a converging vector quantization algorithm that sorts observations into an integer number,  $k$ , of clusters<sup>18</sup> and has been implemented for analysis of 4D STEM data<sup>19</sup> and x-ray nanodiffraction of ferroelectric thin films.<sup>20</sup> Following a standard Python implementation of the algorithm<sup>21</sup> with each pixel on the x-ray detector as an “observation” and each position in an area map as a “feature,” we clustered the pixels into groups representing different portions of the scattering signal.

Taking the minimum inertia (sum of squared Euclidean distances of observations to their closest cluster center) result of k-means clustering with 9000 randomized centroid initiations, we grouped the diffraction signal into four clusters [Fig. 2(a)], which are orthogonal by nature due to their non-overlapping coordinates in the reciprocal space. Figure 2(b) depicts the clusters in the three-dimensional space, with the axes given by the first three principal components of the data. Principal component analysis (PCA) is another example of dimensionality reduction with orthonormal principal components and can be used to evaluate the quality of clustering.<sup>22</sup> In our case, the four clusters are distinguishable from the PCA condensation of  $81 \times 81$  measurements (dimensions) of  $63 \times 63$  pixels (raw data binned, combining  $4 \times 4$  pixels into 1) into three dimensions. Clusters 1 and 2 [Figs. 2(c) and 2(d)] consist of signals from the donut-shaped zone plate reflection on the Bragg peak, representing scattering from the perfect crystalline lattice. The shift to higher  $2\theta$  (measured as the horizontal position on the area detector) from cluster 1 to cluster 2 indicates a slight tilt or a strain gradient in the lattice planes, indistinguishable using single angle diffraction. The lines below the ring occur

due to parasitic illumination from imperfections in the focusing optics. Cluster 3 is diffuse (less structured and broader in the reciprocal space), and notably, the first and third principal components [Fig. 2(b)] shows the separation of Bragg and diffuse scattering, confirming the results of labeling by k-means. Cluster 4 [Fig. 2(f)] shows no structure, and we attribute it to the background noise. The noise intensity is comparable to the diffuse scattering intensity, demonstrating the algorithm’s strength in interpreting noisy data. Furthermore, the background cluster serves as a guideline for the number of clusters used to classify the scattering signal; increasing the number of clusters,  $k$ , results in the separation of the background signal into different clusters (Figs. S6 and S8), a result with no physical grounding.

To relate the different portions of the scattering signal to the positions of nano-scale lattice distortions in the film, we created a binary mask for each cluster [Figs. 2(c)–2(f), top], which represents a distinct portion of the reciprocal space. The pixel positions given by specified cluster labels were assigned a value of 1, while all other pixels (belonging to different clusters) were set to 0. We then applied this binary mask pointwise to the raw diffraction data, thereby isolating each cluster’s signal into a series of corresponding spatial maps [Figs. 2(c)–2(f), bottom]. This procedure is reminiscent of dark-field imaging except that the unsupervised k-means clustering determines the regions of the masks from the 4D diffraction data. The maps corresponding to clusters 1 and 2 represent regions with high crystallinity and have similar integrated intensities. The slight shift in the reciprocal space indicates a strain gradient or tilt across the top-right corner of the mapped region. The map corresponding to cluster 3 reveals localized lattice distortions as diffuse scattering arises from crystal distortions or defects.<sup>23</sup> Notably, the map of cluster 3 is anti-correlated with both maps from clusters 1 and 2 (perfect crystal): each measured location on the film generates either Bragg or diffuse scattering.

Varying the incident angle allows us to measure the distribution of the diffuse scattering in the reciprocal space and its corresponding dark-field maps in the real space. At the Bragg condition, the spread of

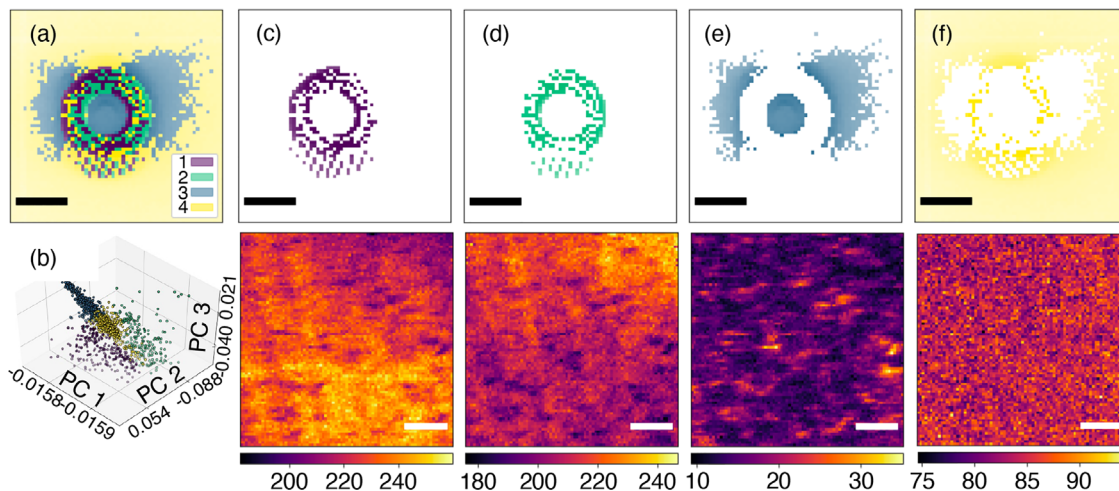


**FIG. 2.** (a) Cluster labels for each detector pixel of diffraction at the SrIrO<sub>3</sub> 002<sub>pc</sub> Bragg angle ( $\theta = 15.87^\circ$ ) using k-means++ centroid initiation. (b) Cluster labels plotted along the first three principal components. (c)–(f) Each cluster (top) and corresponding  $5 \times 5 \mu\text{m}^2$  spatial map (bottom) generated by the integrated intensity from pointwise multiplication of a binary mask of the cluster and the full diffraction image at each point of the scan.  $2\theta$  is in the horizontal direction, and the scale bar for all diffraction clusters is  $0.22^\circ$ , while the scale bar for all spatial maps is  $1 \mu\text{m}$ . The false color intensity maps have units of photons/s (count reduced by a factor of 16 due to binning).

diffuse scattering is centered around the donut-shaped Bragg peak [Fig. 2(e)]. Thus, a significant portion of the measurable diffuse scattering overlaps with the reflection of the Fresnel zone plate. Figure 3 shows the resulting diffuse scattering isolated via k-means clustering (other clusters shown in Fig. S5 of the [supplementary material](#)) from scans collected offset from the Bragg peak by  $\Delta\theta = \pm 0.2^\circ$  [data in Fig. 1(c)]. The spatial maps found through k-means clustering at different angles are correlated, confirming that the same spatial region of the sample was measured at different angles and that the broad diffuse scattering is visible at off-Bragg angles. Nevertheless, nuanced differences appear: the integrated intensity of the diffuse scattering at the Bragg condition is higher than in both off-Bragg measurements suggesting that the diffuse scattering is maximized at the Bragg angle and reduces when scanned perpendicularly to Q. The strength of cluster analysis is further highlighted through the similarity across all three dark-field images in Fig. 3: although the diffuse cluster in the on-Bragg scan contains intensity contribution from optics-induced parasitic

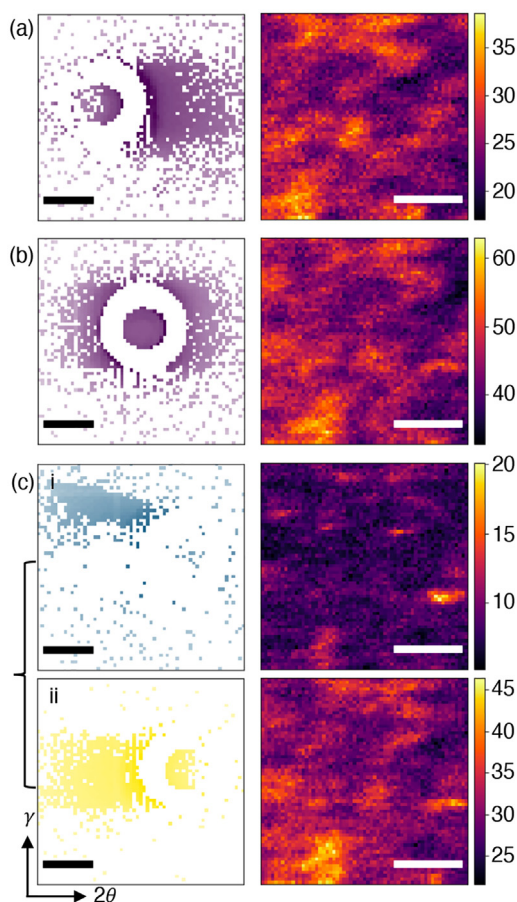


**FIG. 3.** Diffuse scattering identified via k-means clustering (left) of measurements at  $\theta = 15.67^\circ$  (a),  $\theta = 15.87^\circ$  (b), and  $\theta = 16.07^\circ$  (c), and the corresponding integrated intensity maps (right) of the pristine  $\text{SrIrO}_3$  film. In (i), the diffuse scattering is concentrated in the higher  $\gamma$ , and in (ii), it is spread along the direction of the scattering vector. The scalebar for diffuse clusters (left) is  $0.22^\circ$ , and the scale bar for spatial maps (right) is  $1 \mu\text{m}$ . The false color intensity maps have units of photons/s (count reduced by a factor of 16 due to binning).

illumination, it still identifies the same features as in the other two scans with relatively low overlap. Additionally, k-means clustering can be applied to categorize differences within the diffuse scattering at a particular scattering condition [Fig. 3(c)]: the intensity away from the crystal truncation rod distributed perpendicular to the scattering vector indicates in-plane lattice disorder.<sup>24,25</sup>

While the current data are insufficient to definitively identify the observed lattice distortions, we can use their spatial distribution and their signal in the reciprocal space to investigate their origin. In epitaxial thin films, local lattice distortions can arise from point defects, yet localized strain due to point defects is likely too small to be imaged by a hard x-ray nanoprobe. Other possible explanations of the observed lattice distortions are threading dislocations and dislocation half-loops, extensively studied in epitaxial semiconductor thin films<sup>26,27</sup> and other functional oxides.<sup>28,29</sup> In heteroepitaxial systems with highly mismatched lattices, misfit dislocations nucleate at the substrate–film interface and propagate normal to the film–air interface. In  $\text{SrIrO}_3$  grown on LSAT, a system with a relatively low mismatch, half-loops are more likely to nucleate at the film surface and undergo dislocation climb to the substrate–film interface during growth.<sup>30</sup> Measurement of an asymmetric peak with an in-plane component confirms that the film is commensurately strained [Fig. S1(c)] and, thus, does not have appreciable density of misfit dislocations. Nonetheless, there is a high concentration ( $\sim 10^4 \text{ cm}^{-1}$ ) of dislocation half loops in epitaxial systems of similar strain<sup>31,32</sup> as well as dislocations and other defects from the substrate crystal, both of which affect local structure and thus scattering intensity in the film.

In the pristine films, the bright regions in Fig. 2(e) (bottom) correspond to areas of relatively high integrated diffuse scattering intensity. These features are several tens to hundreds of nanometers in scale, which correlates well with the expected extension of strain effects due to dislocations. The latter have an average separation of about several hundreds of nm to  $1 \mu\text{m}$ ,<sup>31,32</sup> accounting for the ability to probe the entire thickness of the film with x rays. We only measured the  $002_{\text{pc}}$  specular reflection sensitive to lattice displacement along  $[002]_{\text{pc}}$ . Nonetheless, because edge and mixed dislocations produce strain fields both along the dislocation Burgers vector and perpendicular to it,<sup>33</sup> the stress induced by such an internal dislocation is relieved into both in-plane and out-of-plane constants locally relative to a fixed Poisson ratio for the unit cell. Thus, our measurements are sensitive to their presence despite the reflection choice. We cannot completely rule out other origins for localized crystal distortions. Nevertheless, the homogeneous distribution of the fluorescence signal (see Figs. S2–S4) indicates the absence of large changes in Ir concentrations or impurities on the surface.

While understanding localized structural heterogeneities in as-grown films provides an important baseline measurement, the greater challenge lies in observing defects in electrochemically cycled  $\text{SrIrO}_3$  films. During the OER in alkaline electrocatalysis,  $\text{SrIrO}_3$  adsorbs and transforms surface species from the active  $\text{Ir}^{4+}$  sites,<sup>34</sup> changing the local structure of the film surface and immediate sub-surface layers.<sup>35</sup> Thus, by comparing the heterogeneities between pristine and cycled  $\text{SrIrO}_3$  films, we can infer the potential morphology rearrangements during the OER electrocatalysis on  $\text{SrIrO}_3$ . Figure 4(a) shows the six clusters resulting from 3000 initiations of k-means clustering, performed on data collected from an alkaline-treated  $\text{SrIrO}_3$  film (see [supplementary material](#), Methods). Four clusters correspond to signal

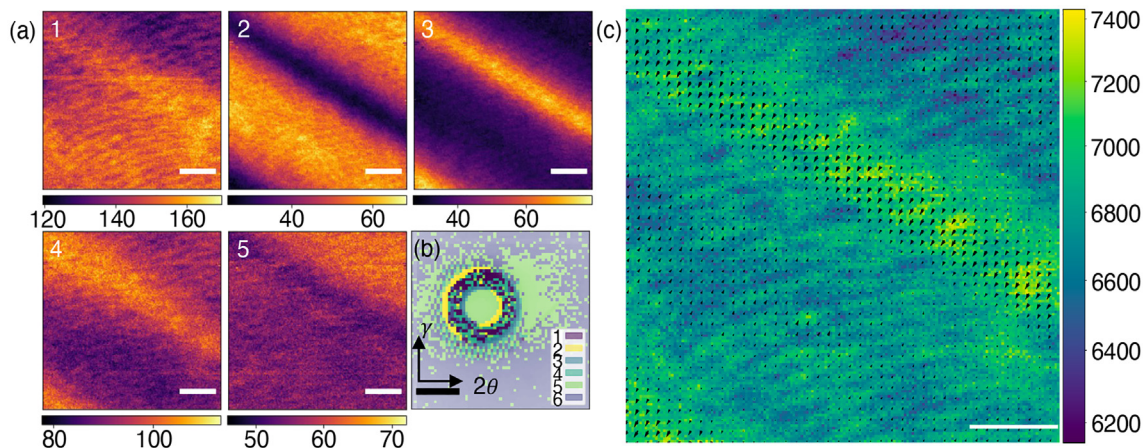


**FIG. 4.** (a) (1–5) Corresponding intensity maps to the clusters [(b), bottom right]. Cluster 6, the background noise, is omitted for brevity. (b) Clusters of the nanodiffraction pattern of the electrochemically cycled film collected at the  $\text{SrIrO}_3$   $002_{pc}$  Bragg condition, with the scale bar indicating  $0.22^\circ$ . (c) Integrated intensity map of  $\text{SrIrO}_3$   $002_{pc}$  of the film cycled electrochemically in 0.1 M KOH, with arrows indicating the simulated direction and relative magnitude of lattice plane tilt. All maps show the same  $10 \times 10 \mu\text{m}^2$  measured region (map scalebar =  $2 \mu\text{m}$ ). The false color intensity maps have units of photons/s (count in cluster maps reduced by a factor of 16 due to binning).

from the Bragg peak. The map corresponding to cluster 5 highlights the features present in the diffuse scattering. Although the primary contribution to the difference in the scattering intensity concentrates across the stripe running diagonally downward from the upper left corner of the measured region, smaller lines are present at an angle to the larger ones. These features are also shown across the four clusters representing different portions of the Bragg peak, particularly the two wider diagonal stripes of relatively high intensity.

Although we cannot directly compare the same region of one sample before and after electrochemical cycling in this study, the measurements before and after differ visibly in morphology. While we identify defects in the as-grown  $\text{SrIrO}_3$  film as oblong spots 200–300 nm in the broad direction, intensity modulations in the alkaline-treated film takes the form of stripes with 600 nm periodicity (Fig. S8). These heterogeneities could be due to a number of factors, including dislocations, amorphization of the surface after electrochemical cycling,<sup>35</sup> or uneven film thickness. The featureless Ir fluorescence trace (Fig. S4) confirms that this difference in morphology is due to complex structure within the Bragg peak and extended defects rather than Ir inclusions or cracking of the brittle film. This complex structure highlights the need for analysis methods beyond manual dark-field imaging processing,<sup>14</sup> as the subtle differences within the donut-shaped zone plate reflection shown through k-means clustering are impossible to identify and discern manually. The two larger stripes originating from the signal in clusters 2 and 3 [Figs. 4(a-2), 4(a-3), and 4(b)] represent either a tilt or strain gradient, which are indistinguishable in a single Ewald sphere measurement; however, the local strain, tilt, and thickness can be simulated with known sample and experimental geometry parameters (simulations, Fig. S9 of the [supplementary material](#)).<sup>36</sup> As shown in Fig. 4(c), the large stripes correspond to regions with tilted lattice planes ( $\sim 0.01^\circ$  in the vertical direction and  $\sim 0.007^\circ$  in the horizontal direction), likely due to the miscut of the LSAT substrate crystal. Clusters 2 and 3 as well as the simulated diffraction (Fig. S9) demonstrate how the position of the zone plate

image changes in the reciprocal space due to lattice rotations. Notably, the intensity corresponding to the Bragg peak [Figs. 4(a-1)–4(a-4)] is not two orders of magnitude higher than that of the diffuse scattering [Fig. 4(a-5)] as in the pristine sample [Figs. 2(c)–2(e)]. Within all measured regions of both the as-grown (four regions of between  $3 \times 3$  and  $5 \times 5 \mu\text{m}^2$ ) and electrochemically cycled samples (three regions), the fine striped structure was only observed throughout the cycled film (Fig. S6 of the [supplementary material](#)). Nevertheless, we compared two different sample regions, which highlight a fundamental flaw in *ex situ* measurements—the inability to monitor structural changes in response to an external driving force—and emphasize the necessity of *operando* measurements.

In this study, we combined unsupervised k-means clustering with scanning x-ray nanodiffraction to identify and characterize defect and strain behavior from the diffuse scattering produced by as-grown and alkaline-treated  $\text{SrIrO}_3$  epitaxial thin films. We measured localized distortions from the ideal crystalline lattice in pristine films and observed that the defect morphology is different in electrochemically cycled films. Additionally, the presented work demonstrates the potential that unsupervised machine learning applied to the 4D x-ray nanodiffraction datasets has for isolating low-intensity diffuse scattering signal and subtle changes within the Bragg peak. We anticipate that the approach shown will serve as a methodology to monitor localized morphological changes and their role in electrochemical reactions in the future.

See the [supplementary material](#) for materials synthesis, electrochemical cycling, x-ray nano-diffraction parameters, and additional results.

The authors acknowledge Dr. Ludi Miao for his help in lithography of fiducials and Matthew Barone for in-house reciprocal space mapping. This work was primarily supported as part of the Center for Alkaline Based Energy Solutions (CABES), an Energy Frontier Research Center funded by the U.S. Department of

Energy, Office of Science, Basic Energy Sciences at Cornell under Award No. DE-SC0019445 (A.L., O.Yu.G., Z.S., D.-Y.K., R.B., J.S., and A.S.). A.L. acknowledges a graduate research fellowship through the National Science Foundation (No. DGE-2139899). Use of the Advanced Photon Source and the Center for Nanoscale Materials, both Office of Science User Facilities, was supported by the U.S. Department of Energy, Office of Science, Office of Basic Energy Sciences, under Contract No. DE-AC02-06CH11357. The thin film synthesis was supported by the National Science Foundation [Platform for the Accelerated Realization, Analysis, and Discovery of Interface Materials (PARADIM)] under Cooperative Agreement No. DMR-2039380 (J.N.N., K.M.S., and D.G.S.). This work was performed in part at the Cornell NanoScale Facility (CNF), a member of the National Nanotechnology Infrastructure Network, which was supported by the NSF (Grant No. ECCS-0335765).

## AUTHOR DECLARATIONS

### Conflict of Interest

The authors have no conflicts to disclose.

### Author Contributions

**Aileen Luo:** Data curation (equal); Formal analysis (lead); Methodology (lead); Visualization (lead); Writing – original draft (lead); Writing – review & editing (lead). **Kyle M. Shen:** Methodology (supporting); Resources (supporting). **Darrell G. Schlom:** Conceptualization (supporting); Methodology (supporting); Resources (supporting); Writing – review & editing (supporting). **Jin Suntivich:** Conceptualization (supporting); Methodology (supporting); Resources (supporting); Writing – review & editing (supporting). **Andrej Singer:** Conceptualization (lead); Data curation (equal); Formal analysis (supporting); Funding acquisition (lead); Investigation (equal); Methodology (equal); Project administration (equal); Resources (lead); Supervision (lead); Writing – review & editing (supporting). **Oleg Gorobtsov:** Conceptualization (supporting); Data curation (equal); Formal analysis (supporting); Investigation (supporting); Methodology (supporting); Writing – review & editing (supporting). **Jocienne Nelson:** Investigation (supporting); Methodology (supporting); Resources (supporting). **Ding-Yuan Kuo:** Investigation (supporting); Methodology (supporting); Resources (supporting). **Tao Zhou:** Formal analysis (supporting); Methodology (supporting); Software (equal); Validation (supporting); Visualization (supporting); Writing – review & editing (supporting). **Ziming Shao:** Investigation (supporting); Methodology (supporting). **Ryan Bouck:** Investigation (supporting). **Mathew J. Cherukara:** Investigation (supporting); Methodology (equal); Resources (equal). **Martin V. Holt:** Investigation (supporting); Methodology (equal); Resources (equal).

### DATA AVAILABILITY

The data that support the findings of this study are available from the corresponding author upon reasonable request.

### REFERENCES

<sup>1</sup>Y. Jia, K. Jiang, H. Wang, and X. Yao, *Chem* **5**, 1371 (2019).

- <sup>2</sup>W. T. Hong, M. Risch, K. A. Stoerzinger, A. Grimaud, J. Suntivich, and Y. Shao-Horn, *Energy Environ. Sci.* **8**, 1404 (2015).
- <sup>3</sup>E. Herrero, K. Franaszczuk, and A. Wieckowski, *J. Phys. Chem.* **98**, 5074 (1994).
- <sup>4</sup>R. Gao, A. Fernandez, T. Chakraborty, A. Luo, D. Pesquera, S. Das, G. Velarde, V. Thoréton, J. Kilner, T. Ishihara, S. Nemsák, E. J. Crumlin, E. Ertekin, and L. W. Martin, *Adv. Mater.* **33**, 2100977 (2021).
- <sup>5</sup>C. J. Eom, D. Y. Kuo, C. Adamo, E. J. Moon, S. J. May, E. J. Crumlin, D. G. Schlom, and J. Suntivich, *Nat. Commun.* **9**, 1 (2018).
- <sup>6</sup>J. W. Hall and H. F. Rase, *Nature* **199**, 585 (1963).
- <sup>7</sup>A. Singer, M. Zhang, S. Hy, D. Cela, C. Fang, T. A. Wynn, B. Qiu, Y. Xia, Z. Liu, A. Ulvestad, N. Hua, J. Wingert, H. Liu, M. Sprung, A. V. Zozulya, E. Maxey, R. Harder, Y. S. Meng, and O. G. Shpyrko, *Nat. Energy* **3**, 641 (2018).
- <sup>8</sup>S. Hwang, X. Chen, G. Zhou, and D. Su, *Adv. Energy Mater.* **10**, 1902105 (2020).
- <sup>9</sup>Y. Yuan, K. Amine, J. Lu, and R. Shahbazian-Yassar, *Nat. Commun.* **8**, 15806 (2017).
- <sup>10</sup>D. Markovich, M. Zachman, S.-H. Yu, R. Selhorst, T. Moon, H. Abruña, K. Noonan, and L. Kourkoutis, *Microsc. Microanal.* **26**, 1648 (2020).
- <sup>11</sup>W. Yu, H. J. Fu, T. Mueller, B. S. Brunschwig, and N. S. Lewis, *J. Chem. Phys.* **153**, 020902 (2020).
- <sup>12</sup>M. R. Nellist, F. A. L. Laskowski, J. Qiu, H. Hajibabaei, K. Sivula, T. W. Hamann, and S. W. Boettcher, *Nat. Energy* **3**, 46 (2018).
- <sup>13</sup>R. Ye, M. Zhao, X. Mao, Z. Wang, D. A. Garzón, H. Pu, Z. Zhao, and P. Chen, *Nat. Commun.* **12**, 4287 (2021).
- <sup>14</sup>A. Singer, J. G. Ramirez, I. Valmianski, D. Cela, N. Hua, R. Kukreja, J. Wingert, O. Kovalchuk, J. M. Glowina, M. Sikorski, M. Chollet, M. Holt, I. K. Schuller, and O. G. Shpyrko, *Phys. Rev. Lett.* **120**, 207601 (2018).
- <sup>15</sup>L. C. Seitz, C. F. Dickens, K. Nishio, Y. Hikita, J. Montoya, A. Doyle, C. Kirk, A. Vojvodic, H. Y. Hwang, J. K. Nørskov, and T. F. Jaramillo, *Science* **353**, 1011–1014 (2016).
- <sup>16</sup>R. Tang, Y. Nie, J. K. Kawasaki, D. Y. Kuo, G. Petretto, G. Hautier, G. M. Rignanese, K. M. Shen, D. G. Schlom, and J. Suntivich, *J. Mater. Chem. A* **4**, 6831 (2016).
- <sup>17</sup>R. P. Winarski, M. V. Holt, V. Rose, P. Fuesz, D. Carbaugh, C. Benson, D. Shu, D. Kline, G. B. Stephenson, I. McNulty, and J. Maser, *J. Synchrotron Radiat.* **19**, 1056 (2012).
- <sup>18</sup>S. P. Lloyd, *IEEE Trans. Inf. Theory* **28**, 129 (1982).
- <sup>19</sup>S. Jesse, M. Chi, A. Belianinov, C. Beekman, S. V. Kalinin, A. Y. Borisevich, and A. R. Lupini, *Sci. Rep.* **6**, 26348 (2016).
- <sup>20</sup>J. Christiansen-Salameh, M. Yang, G. Rippey, J. Li, Z. Cai, M. Holt, G. Agnus, T. Maroutian, P. Lecoeur, S. Matzen, and R. Kukreja, *J. Synchrotron Radiat.* **28**, 207 (2021).
- <sup>21</sup>F. Pedregosa, G. Varoquaux, A. Gramfort, V. Michel, B. Thirion, O. Grisel, M. Blondel, A. Müller, J. Nothman, G. Louppe, P. Prettenhofer, R. Weiss, V. Dubourg, J. Vanderplas, A. Passos, D. Cournapeau, M. Brucher, M. Perrot, and É. Duchesnay, *J. Mach. Learn. Res.* **12**, 2825 (2011).
- <sup>22</sup>G. W. Stewart, *SIAM Rev.* **35**, 551 (1993).
- <sup>23</sup>B. E. Warren, *X-Ray Diffraction* (Dover Publications, 1990).
- <sup>24</sup>I. K. Robinson, *Phys. Rev. B* **33**, 3830 (1986).
- <sup>25</sup>A. S. Disa, F. J. Walker, and C. H. Ahn, *Adv. Mater. Interfaces* **7**, 1901772 (2020).
- <sup>26</sup>C. Yildirim, P. Ballet, J. L. Santailier, D. Giotta, R. Obrecht, T. N. T. Thi, J. Baruchel, and D. Brellier, *J. Synchrotron Radiat.* **28**, 301 (2021).
- <sup>27</sup>M. Barchuk, V. Holý, and D. Rafaja, *J. Appl. Phys.* **123**, 161552 (2018).
- <sup>28</sup>X. Shen, T. Yamada, R. Lin, T. Kamo, H. Funakubo, D. Wu, H. L. Xin, and D. Su, *Appl. Phys. Lett.* **107**, 141605 (2015).
- <sup>29</sup>I. Vrejoiu, G. Le Rhun, N. D. Zakharov, D. Hesse, L. Pintilie, and M. Alexe, *Philos. Mag.* **86**, 4477 (2006).
- <sup>30</sup>L. B. Freund and S. Suresh, *Thin Film Materials* (Cambridge University Press, 2004).
- <sup>31</sup>H. P. Sun, X. Q. Pan, J. H. Haeni, and D. G. Schlom, *Appl. Phys. Lett.* **85**, 1967 (2004).

- <sup>32</sup>E. Navickas, Y. Chen, Q. Lu, W. Wallisch, T. M. Huber, J. Bernardi, M. Stöger-Pollach, G. Friedbacher, H. Hutter, B. Yildiz, and J. Fleig, *ACS Nano* **11**, 11475 (2017).
- <sup>33</sup>D. Hull and D. J. Bacon, *Introduction to Dislocations* (Elsevier, 2011), pp. 63–83.
- <sup>34</sup>D. Y. Kuo, C. J. Eom, J. K. Kawasaki, G. Petretto, J. N. Nelson, G. Hautier, E. J. Crumlin, K. M. Shen, D. G. Schlom, and J. Suntivich, *J. Phys. Chem. C* **122**, 4359 (2018).
- <sup>35</sup>G. Wan, J. W. Freeland, J. Kloppenburg, G. Petretto, J. N. Nelson, D. Y. Kuo, C. J. Sun, J. Wen, J. T. Diulus, G. S. Herman, Y. Dong, R. Kou, J. Sun, S. Chen, K. M. Shen, D. G. Schlom, G. M. Rignanes, G. Hautier, D. D. Fong, Z. Feng, H. Zhou, and J. Suntivich, *Sci. Adv.* **7**, eabc7323 (2021).
- <sup>36</sup>M. Holt, R. Harder, R. Winarski, and V. Rose, *Annu. Rev. Mater. Res.* **43**, 183 (2013).

**Supporting Information**  
**X-ray Nano-Imaging of Defects in Thin Film Catalysts via Cluster Analysis**

Aileen Luo<sup>1</sup>, Oleg Yu. Gorobtsov<sup>1</sup>, Jocienne N. Nelson<sup>2</sup>, Ding-Yuan Kuo<sup>1</sup>, Tao Zhou<sup>3,4</sup>, Ziming Shao<sup>1</sup>, Ryan Bouck<sup>1</sup>, Mathew J. Cherukara<sup>3,4</sup>, Martin V. Holt<sup>3,4</sup>, Kyle M. Shen<sup>5,6</sup>, Darrell G. Schlom<sup>1,6,7</sup>, Jin Suntivich<sup>1</sup>, Andrej Singer<sup>1</sup>

<sup>1</sup>Department of Materials Science and Engineering, Cornell University

<sup>2</sup>Laboratory of Atomic and Solid State Physics, Department of Physics, Cornell University

<sup>3</sup>Advanced Photon Source, Argonne National Laboratory

<sup>4</sup>Center for Nanoscale Materials, Argonne National Laboratory

<sup>5</sup>Department of Applied and Engineering Physics, Cornell University

<sup>6</sup>Kavli Institute at Cornell for Nanoscale Science, Ithaca, New York 14853, USA

<sup>7</sup>Leibniz-Institut für Kristallzüchtung, Max-Born-Str. 2, 12489 Berlin, Germany

**Experimental Methods**

**Molecular Beam Epitaxy (MBE) Synthesis.** 30 formula units of SrIrO<sub>3</sub> (001)<sub>pc</sub> were grown via reactive oxide molecular beam epitaxy on single-crystal (LaAlO<sub>3</sub>)<sub>0.3</sub>(SrAl<sub>0.5</sub>Ta<sub>0.5</sub>O<sub>3</sub>)<sub>0.7</sub> (001) (LSAT, CrysTec), providing a high quality epitaxial growth (see Fig. S1A). There is a 1.9% average in-plane compressive strain on the film. In situ reflection high-energy electron diffraction (RHEED) (see Fig. S1B,C) confirmed layered epitaxial growth with RHEED oscillations used to monitor film thickness. A thermocouple measured the substrate temperature as 650 °C. The distilled ozone oxidant pressure (80% O<sub>3</sub>+20% O<sub>2</sub>) was 10<sup>-6</sup> Torr, and a quartz crystal microbalance was used to calibrate Ir flux supplied by an electron beam evaporator. A Sr flux of 1x10<sup>13</sup> atoms cm<sup>-2</sup>s<sup>-1</sup> was supplied by a low-temperature effusion cell, with a Sr/Ir ratio of 0.82. More details on the growth may be found in the references<sup>1,2</sup>.

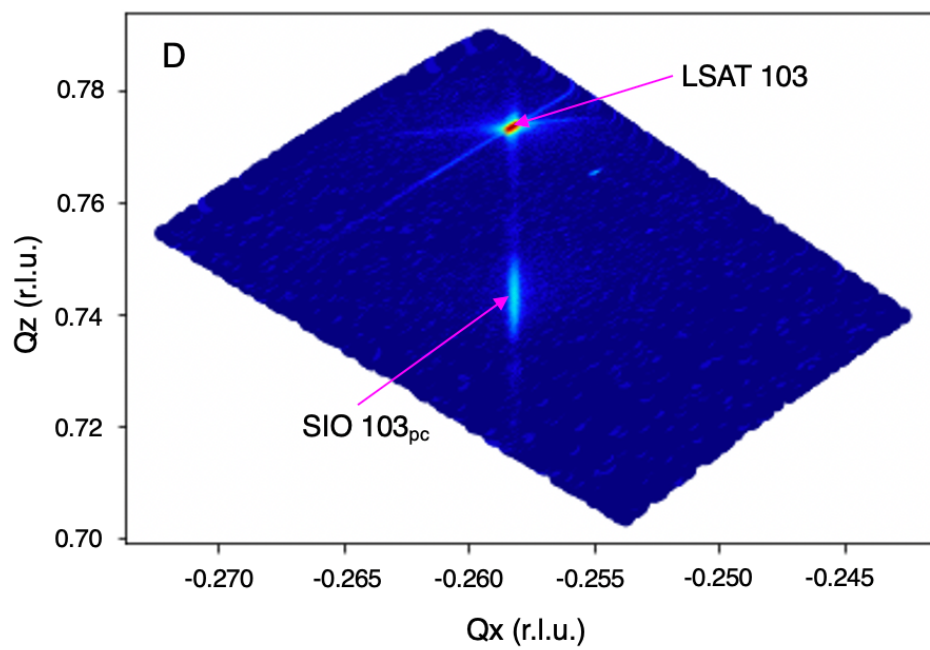
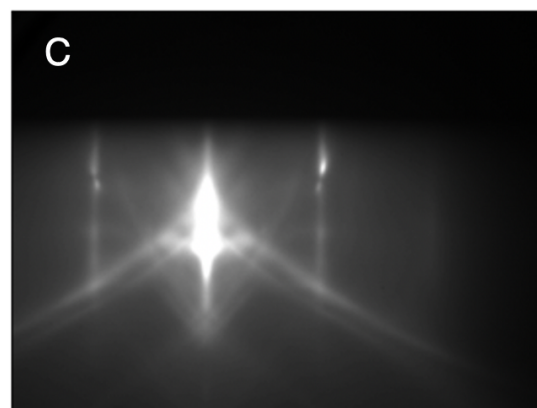
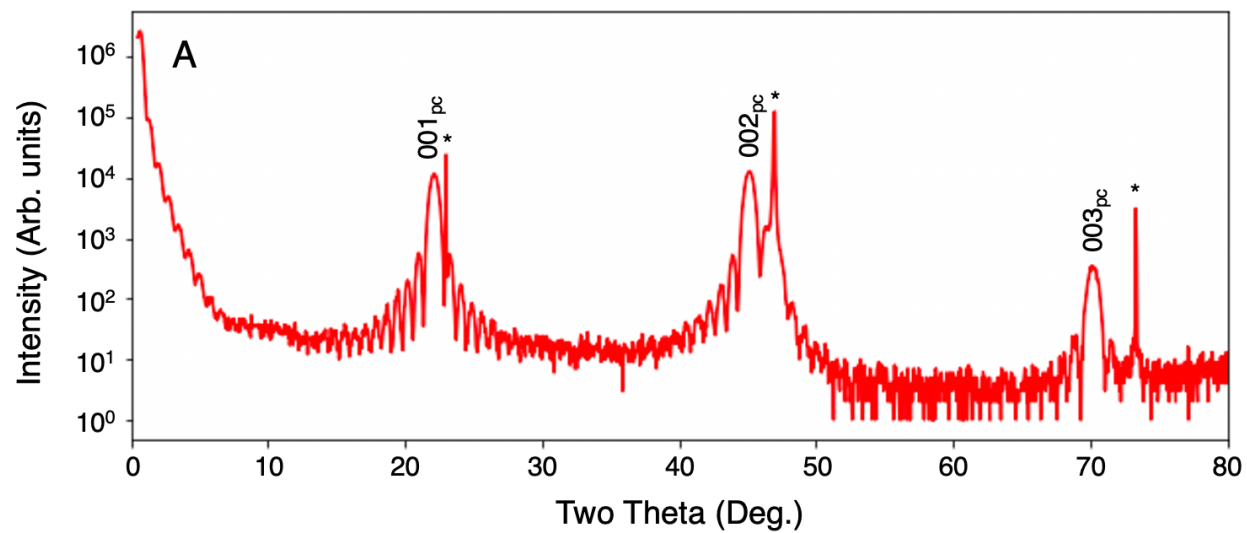


**Figure S1.** A) X-ray diffraction of the SrIrO<sub>3</sub> (SIO) thin film taken using Cu-K<sub>α</sub> radiation. The film peaks are labeled using their pseudo-cubic indices (denoted by pc). The stars indicate the LSAT 001, 002, and 003 substrate peaks. B,C) Reflection high energy electron diffraction (RHEED) images taken along the film B) [100]<sub>pc</sub> and C) [110]<sub>pc</sub> directions at the end of growth. D) Reciprocal space map around the asymmetric 103<sub>pc</sub> peak, indicating that the film is coherently strained.

**Electrochemical Cycling.** Electrical contacts were made according to previously reported methods<sup>3</sup>. A three-electrode glass cell (Pine) with Ag/AgCl (Pine) calibrated to the H<sub>2</sub> redox as the reference electrode and a Pt wire as the counter electrode was used for all electrochemical testing. The electrolyte was 0.1 M potassium hydroxide (KOH) solution prepared by dissolving KOH pellets (99.99% purity, Sigma-Aldrich) in deionized water (18.2 M Ω cm). Cyclic voltammetry was conducted with a potentiostat (Bio-Logic) in Ar-saturated electrolytes at a scan rate of 200 mV/s and in O<sub>2</sub>-saturated electrolytes at 10 mV/s at room temperature.

**X-ray Nano-probe Diffraction.** All scanning X-ray nano-diffraction experiments were conducted at beamline 26-ID at the Advanced Photon Source of Argonne National Laboratory according to previously reported protocols<sup>4</sup>. A liquid-nitrogen cooled Si (111) double crystal monochromator (DCM) was used to achieve high energy resolution ( $\Delta E/E = 1.7 \times 10^{-4}$ ) and tune the x-ray energy to 11.3 keV. A Fresnel zone plate with outside diameter of 133 μm and outermost zone width of 24 nm combined with order sorting aperture was used to focus the collimated x-ray beam to 30 nm (FWHM) diameter with flux of  $\sim 10^9$  photons/s. In the horizontal scanning direction, the projection of the beam onto the sample is 30 nm / sin(θ), where θ is the angle of the incident beam (about 16° for the SrIrO<sub>3</sub> 002<sub>pc</sub> reflection at 11.3 keV). Thus, the horizontal footprint of the beam is 109 nm, while scans shown in Fig. 2 and 4 of the primary text were taken with  $\sim 60$  nm step size, and scans shown in Fig. 3 were taken with 50 nm step size.

### Additional Data

**Fluorescence.** All scans were collected at 11.3 keV, which is above the Ir L-III edge at 11.215 keV. Fluorescence data is measured simultaneously with diffraction data (shown in the main text) using a separate fluorescence detector.

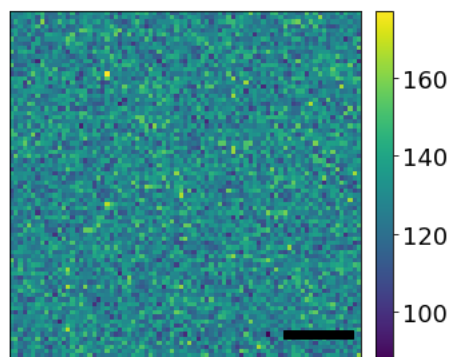


**Figure S2.** Iridium (Ir) fluorescence of the as-grown SIO film. The area shown is the area shown in Figure 2 of the primary text. The scalebar is 1 μm, and the step size in the raster scan is 62.5 nm.

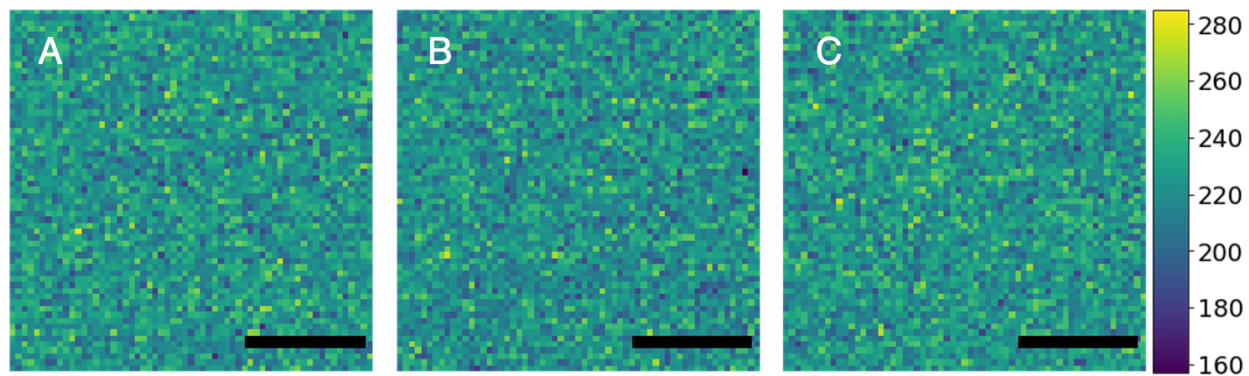


**Figure S3.** Ir fluorescence of the as-grown SIO film, corresponding to the area shown in Figure 3 of the primary text. The scale bar is 1  $\mu\text{m}$  and the step size is 50 nm.

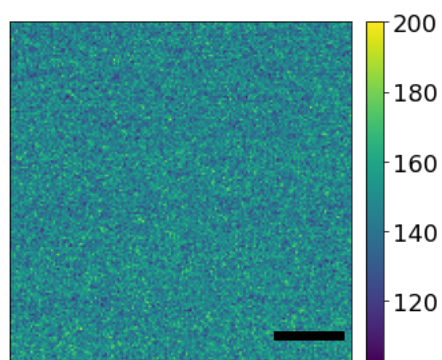


**Figure S4.** Ir fluorescence of the SIO film after electrochemical cycling in 0.1M KOH. The area is the one shown in Figure 4 of the primary text, and the scale bar is 2  $\mu\text{m}$  with 61 nm step size.

## Additional Clustering Results

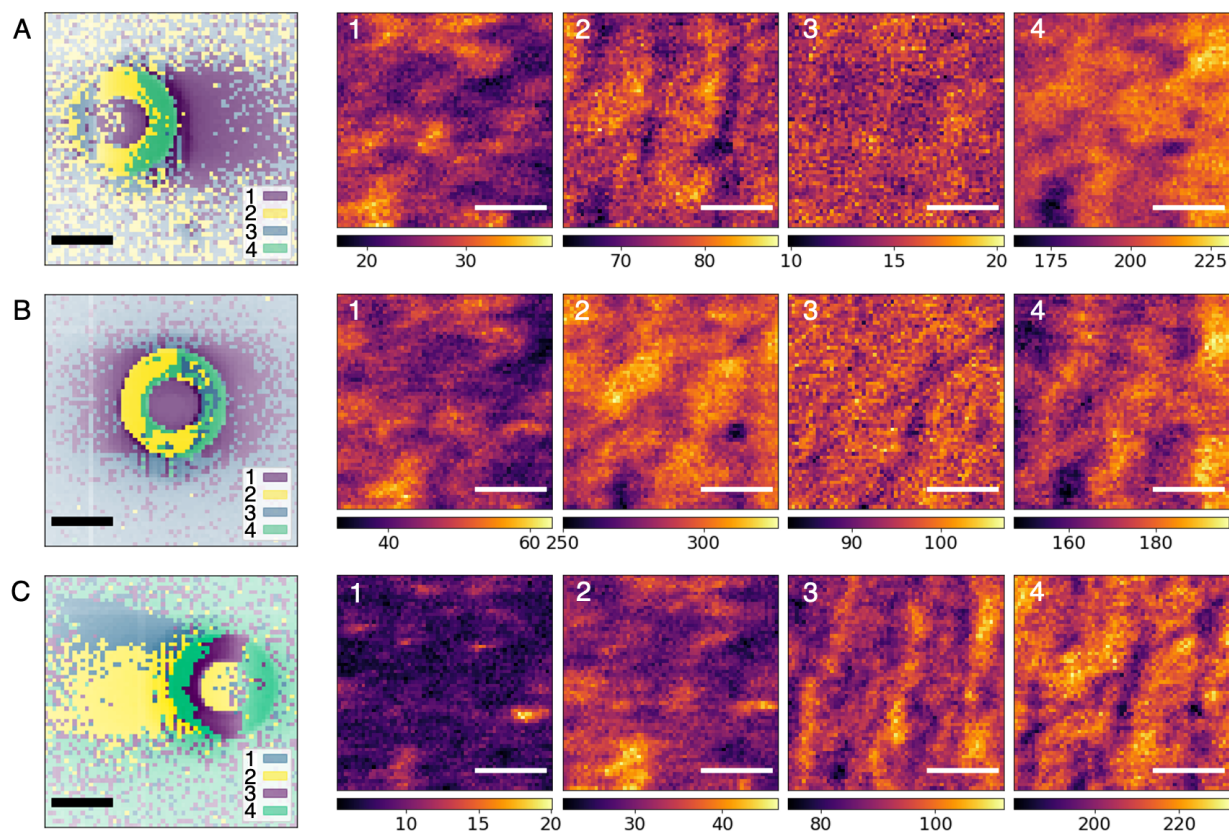


**Figure S5.** Clusters of the nanodiffraction data and their corresponding spatial intensity maps of the as-grown SIO  $002_{pc}$  peak measured at incident beam angles of A)  $\theta = 15.67^\circ$ , B)  $\theta = 15.87^\circ$  (Bragg condition), and C)  $\theta = 16.07^\circ$ . These correspond to Fig. 3A, B, and C, of the primary text, respectively. The black scale bars on the diffraction profiles represent 0.12  $\text{nm}^{-1}$ , while the white scale bars on the maps represent 1  $\mu\text{m}$ .

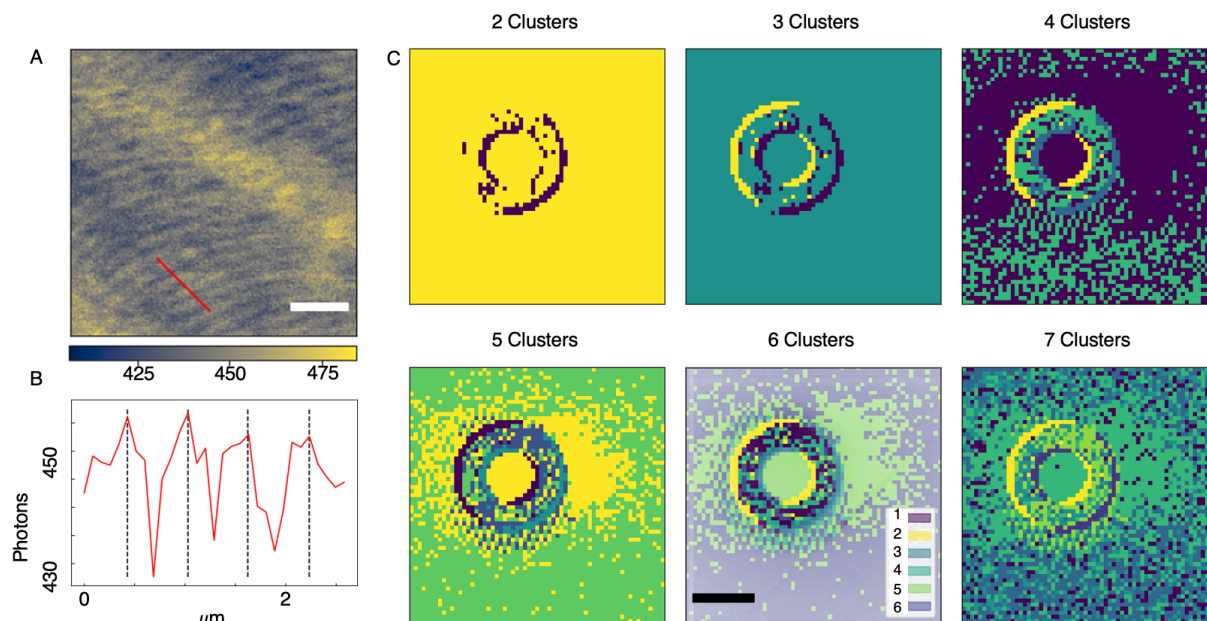


**Figure S6.** *A) Total intensity (binned data) of the electrochemically cycled SrIrO<sub>3</sub> 002<sub>pc</sub> peak (scalebar: 2 μm). B) Line-cut corresponding to the red line in (A) showing the 600 nm periodicity of fine striped structure. C) Clustering results demonstrate the choice of six clusters for the data: adding cluster 7 keeps clusters 1-5 unchanged and splits cluster 6 (background) into two clusters.*

**Large area maps.** Scans of larger step sizes were taken before determining the areas for fine scans. During these coarse scans, diagonal stripes of alternating high and low intensity approximately  $10\ \mu\text{m}$  in periodicity were observed throughout both as-grown and alkaline-treated samples. They run along the film  $[110]_{\text{pc}}$  direction, and we hypothesize that these large features are due to the miscut of the LSAT substrate. While large periodic stripes were observed from both samples (cut from the same crystal), we only found fine striped structures in the electrochemically cycled SIO. Multiple regions in the low-intensity large stripes were measured, but fine structure differed in morphology between the two samples.

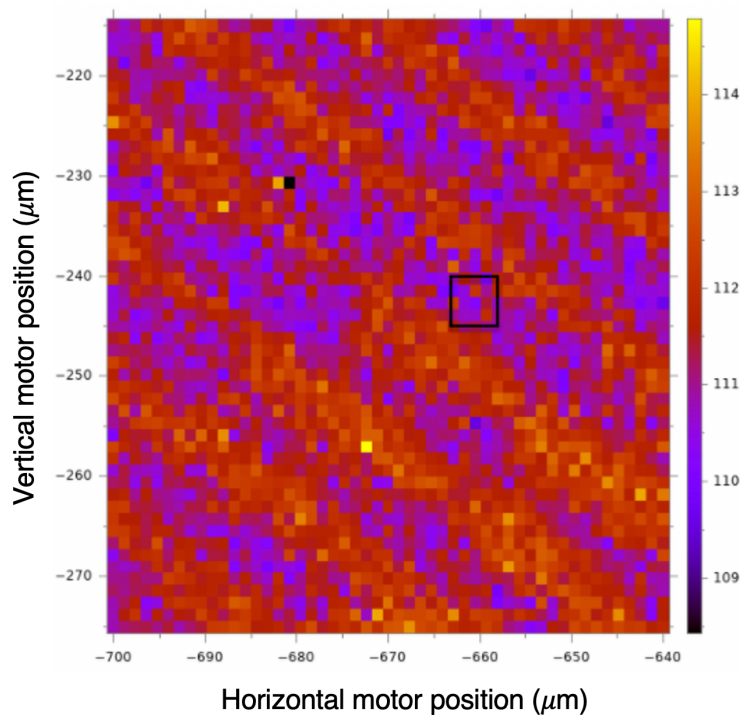


**Figure S7.** The total intensity of a  $60\ \mu\text{m} \times 60\ \mu\text{m}$  area of the as-grown film measured by rastering the sample stage in a plane using coarse motors in the horizontal and vertical directions. The black square indicates the position of the  $5\ \mu\text{m} \times 5\ \mu\text{m}$  area measured and discussed in detail in Fig. 2 of the main text. As seen in Fig. 4 of the text, the large diagonal stripes feature prominently in the alkaline sample as well.

**Clustering code.** For more details about the scripts used, please contact the corresponding author directly.

## Simulations

**K-means.** We simulated a diffraction signal consisting of a donut-shaped peak (corresponding to regions with perfect crystallinity, see Fig. S8A) and a broad Gaussian beam (corresponding to defects, see Fig. S8B), with Poisson noise. We created a raster scan region with mostly perfect crystallinity and 20% defective spots with randomly generated positions. Like the x-ray data, the central peak is two orders of magnitude stronger than the diffuse scattering and we apply Poisson noise comparable to the experiment. We run k-means clustering on the simulated dataset (Fig. S8C shows the total intensity of all simulated diffraction patterns, and Fig. S8D shows the dark field map in real space with dark spots indicating low-intensity defect regions). The clustering algorithm using four clusters identifies all regions with diffuse scattering precisely (see Fig. S8E for clustering results). Note that the donut shaped Bragg peak is split into two clusters, likely because the Poisson noise on the Bragg peak is similar in signal to the diffuse scattering in our simulation. Increasing the signal of the diffuse scattering leads to no splitting of the donut into clusters.

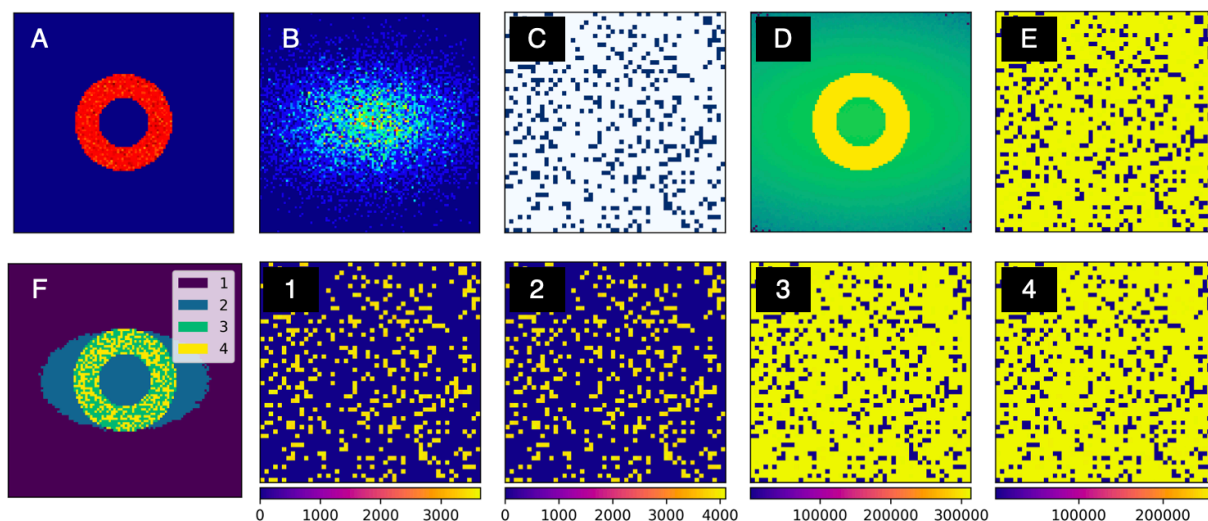


**Figure S8.** Applying *k*-means clustering to simulated Bragg peak with uneven intensity distribution and diffuse scattering, modeled as A) a donut-shaped Bragg peak and B) a gaussian diffuse scattering peak randomly populated onto C) a raster scan with 80 % Bragg and 20 % diffuse scattering spots. D) shows the total scattering intensity of the raster scan and E) is the integrated intensity across a spatial region. F) shows the clusters and 1-4 the spatial maps of the clusters.

**Fitting the lattice tilt.** The position of and intensity distribution across the donut-shaped zone plate image in reciprocal space was simulated. Using known parameters of the epitaxial thin film system, such as film thickness measured during synthesis by RHEED, as well as beamline characterized parameters of the zone plate, the diffraction pattern under different strain and tilt conditions was simulated and used to fit the data. The simulation fits the position of the thickness fringe, the position of the donut in reciprocal space, and the intensity distribution following kinematical theory as a sinc function ( $\text{sinc}(x) = \sin(x)/x$ ), and fits the slice of that sinc function on the Ewald sphere to determine the position of the center of the sinc function in 3D reciprocal space.

The position of the sinc function in reciprocal space allows to determine the strain and tilt of the Bragg planes probed locally with the nanobeam.

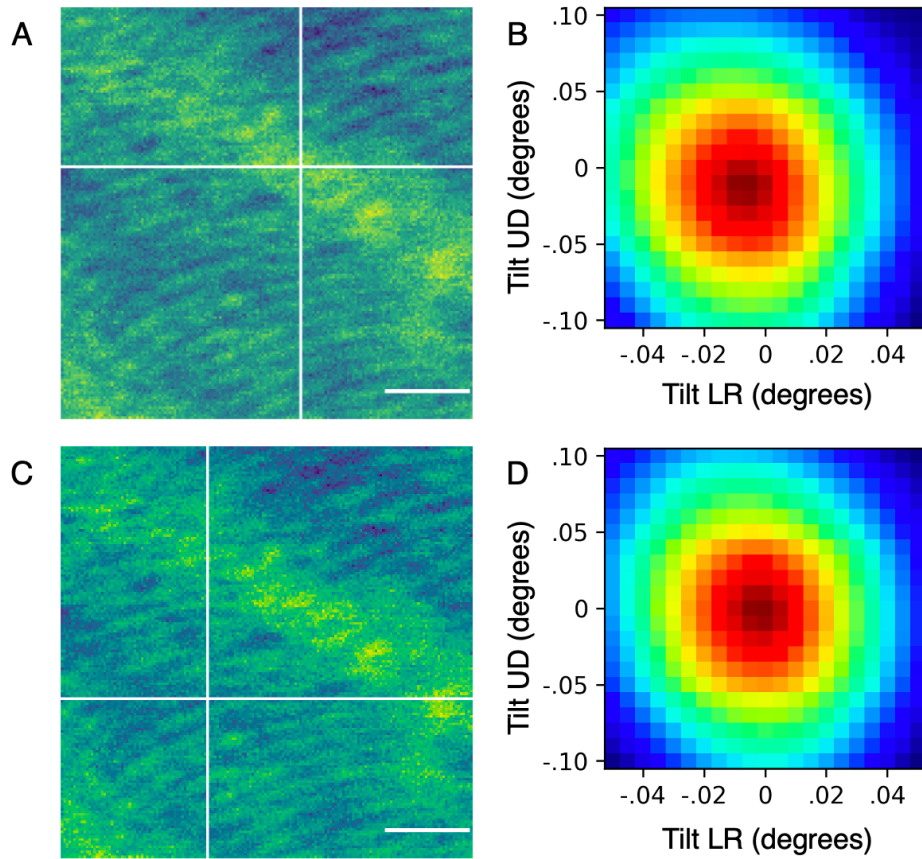


**Figure S9.** A, C) Total intensity of the data with cross-hair indicating a position on the large diagonal stripe of the scan shown in Fig. 4 of the primary text. The scale bar is 2  $\mu\text{m}$ . B, D) Correlation plot of simulated lattice rotation in the left-right (LR) direction (given by  $\tan^{-1}\left(\frac{-Q_x}{-Q_z}\right)$ ) and up-down (UD) direction ( $\sin^{-1}\left(\frac{Q_y}{Q}\right)$ ). The spot in B is further left than the spot in D (visible by a narrow blue stripe at the left edge in D).

## References

1. Nie, Y. F. *et al.* Interplay of Spin-Orbit Interactions, Dimensionality, and Octahedral Rotations in Semimetallic SrIrO<sub>3</sub>. *Phys. Rev. Lett.* **114**, 016401 (2015).
2. Nelson, J. N. *et al.* Mott gap collapse in lightly hole-doped Sr<sub>2-x</sub>K<sub>x</sub>IrO<sub>4</sub>. *Nat. Commun.* **11**, 2597 (2020).
3. Kuo, D. Y. *et al.* Influence of Strain on the Surface-Oxygen Interaction and the Oxygen Evolution Reaction of SrIrO<sub>3</sub>. *J. Phys. Chem. C* **122**, 4359–4364 (2018).
4. Winarski, R. P. *et al.* A hard X-ray nanoprobe beamline for nanoscale microscopy. *J. Synchrotron Radiat.* **19**, 1056–1060 (2012).